Exp Fluids (2011) 51:679–691
DOI 10.1007/s00348-011-1077-3

RESEARCH ARTICLE

The influence of boundary layers on supersonic inlet flow unstart induced by mass injection

Hyungrok Do · Seong-kyun Im · M. Godfrey Mungal · Mark A. Cappelli

Received: 31 August 2010 / Revised: 3 March 2011 / Accepted: 16 March 2011 / Published online: 9 April 2011

Abstract A transverse jet is injected into a supersonic model inlet flow to induce unstart. Planar laser Rayleigh scattering from condensed CO_2 particles is used to visualize flow dynamics during the unstart process, while in some cases, wall pressure traces are simultaneously recorded. Studies conducted over a range of inlet configurations reveal that the presence of turbulent wall boundary layers strongly affect the unstart dynamics. It is found that relatively thick turbulent boundary layers in asymmetric wall boundary layer conditions prompt the formation of unstart shocks; in symmetric boundary conditions lead to the propagation of pseudo-shocks; and in both cases facilitate fast inlet unstart, when compared with thin, laminar boundary layers. Incident shockwaves and associated reflections are found to affect the speed of pressure disturbances. These disturbances, which induce boundary layer separation, are found to precede the formation of unstart shocks. The results confirm the importance of and need to better understand shock-boundary layer interactions in inlet unstart dynamics.

1 Introduction

Inlet unstart has been described as the disgorgement of a shock system at the inlet throat of a scramjet/ramjet engine (Emami et al. 1995). If not avoided, it can cause in-flight engine malfunctioning (Wieting 1976; Hawkins and Marquart 1995; Rodi et al. 1996; Shimura et al. 1998; O'Byrne et al. 2000; Graham 2002; Wagner et al. 2008, 2009). In 1966, a hybrid engine (turbojet and ramjet) powered air fighter (SR-71 Blackbird) capable of Mach 3.2 flight at 80,000 ft crashed due to engine cutoff induced by this inlet unstart (Graham 2002). Most frequently occurring during the transition to ramjet/scramjet mode in the flight Mach number ranges of 3–6 (Andreadis 2004), unstart is believed to be caused by the thermal choking (Mashio et al. 2001) of the internal supersonic flow triggered by increased heat release in the combustor (Heiser and Pratt 1993; Sato et al. 1997; Kodera et al. 2003). The heat release in the combustor is followed by a pressure rise in the inlet duct and boundary layer separation/growth, reducing the core flow area and forcing the internal flow into a subsonic regime (McDaniel and Edwards 2001). Recently, in a ground test facility that mimics the thermal choking by the downstream movement of a mechanical flap, Wagner et al. (2008, 2009a, b) confirmed the presence of the separated boundary layer using particle image velocimetry (PIV) and captured (via high-speed Schlieren photography) the formation and dynamics of an unstart shock system that interacted with the boundary layers. The propagation speed of this unstart shock has been characterized by several researchers and was determined from wall pressure measurements to be in the range of 10–27 m/s in the studies of Wieting (1976), 55–70 m/s in the studies of Rodi et al. (1996), and more recently by Wagner et al. (2009b) in the range of 19–80 m/s.

Past studies have examined methods such as the introduction of isolators (Curran et al. 1996; Sato et al. 1997; Wang and Le 2000; Tam et al. 2008), boundary layer bleeding (Kodera et al. 2003), and vortex generator jets (Valdivia et al. 2009), as a means of avoiding or delaying inlet unstart. The latter two methods seek to influence the

H. Do (✉) · S. Im · M. G. Mungal · M. A. Cappelli
Mechanical Engineering Department, Stanford University, Stanford, CA 94305-3032, USA
e-mail: hyungrok@stanford.edu

M. G. Mungal
School of Engineering, Santa Clara University, Santa Clara, CA 95053, USA

evolution of the boundary layer during the upstream propagation of flow disturbances that originate from the combustor. Recording and understanding the dynamics of boundary layer evolution during unstart are critical to the development of such unstart mitigation strategies. Studies will therefore require diagnostic methods that are capable of resolving the structure of boundary layers and shock-boundary layer interactions.

This paper describes a study of the unstart phenomenon in a supersonic inlet, triggered by mass injection downstream of the inlet. The jet/supersonic flow and ensuing dynamics are highly three dimensional, and we visualize the unstart flow features (e.g., boundary layers, shock-boundary layer interactions) using Planar Laser Rayleigh Scattering (PLRS) from condensed CO_2 particles (particulate fog). Miles and Lempert (1997), Wu et al. (2000), and Poggie et al. (2004) have demonstrated the general utility of this diagnostic for low temperature/pressure supersonic flows expanded through the diverging nozzle of a supersonic wind tunnel of low (ambient) stagnation temperature. Weak (e.g., oblique) shocks are visualized as demarcations in intensity as a result of the post-shock increase in density (and hence particles). However, regions of elevated temperature can cause particle sublimation, and therefore, boundary layers and regions behind strong (normal) shocks lack particles and appear dark, with very strong contrasts. While qualitative at this time, this diagnostic captures flow features with high spatial discrimination (unlike Schlieren photography, which is line-of-sight) and reveals flow dynamics suitable for quantitative characterization, e.g., of regions of boundary layer transition, slip lines, and the propagation of both weak and strong shockwaves.

The use of this PLRS visualization technique allows us to investigate the evolution of fine scale flow structures under unstart flow conditions produced in a model inlet built into a supersonic wind tunnel. The current study reveals that the flow features emerging during unstart are influenced by wall boundary layer conditions, which, in some cases, can either delay or accelerate the inlet unstart process. In addition, the effect of varied jet pressure (proportional to the amount of mass injection into the supersonic flow) and of the presence of incident shockwaves is investigated. Our work is a continuation of initial studies of Do et al. (2010) carried out in the same facility.

2 Experimental setup

The experimental facility consists of a nominally Ma = 5 indraft wind tunnel, an integrated laser system and a jet injection module.

A schematic of the Ma = 5 wind tunnel is shown in Fig. 1. High pressure air (p_0 = 350 kPa and T_0 = 300 K)

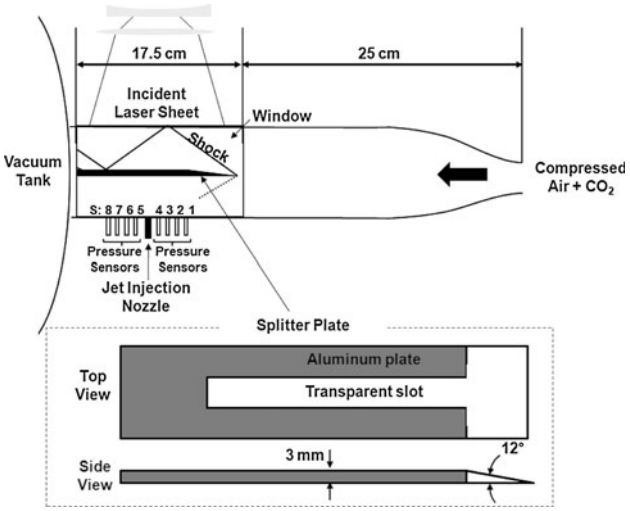

Fig. 1 A schematic of the experimental setup including a Mach 5 wind tunnel, pressure sensors, a splitter plate, and PLRS imaging system

containing CO_2 (approximately 25% by volume) expands through a converging/diverging nozzle (25:1 area ratio) to establish a relatively uniform Ma = 5 flow in a rectangular test section (4 cm × 4 cm cross-sectional area). The exit of the tunnel is connected to a vacuum tank that accommodates the incoming mass flow for approximately 5 s of run time. During this run time, the vacuum tank pressure is maintained at values lower than the static pressure in the test section. A honeycomb of 2.5 cm in length and 3 mm hexagonal cells is placed upstream of the converging nozzle to suppress flow swirling, mostly generated at various junctions in the gas stream inlet piping. The static pressure, temperature, and velocity of the flow in the test section are approximately 1 kPa, 50 K, and 720 m/s, respectively.

A detailed characterization of the variation in Mach number of the flow across the test section is carried out by measuring the shock angle from a sharp leading 12° wedge using Schlieren photography. The measured Mach number midway across the tunnel is Ma = 4.9, with a 5% variation wall to wall (boundary layers were not resolved). Windows on both sides of the test section and transparent upper/lower walls allow optical access. In the baseline configuration, a 3-mm-thick aluminum splitter plate (designed to have a sharp but wedged leading edge and a transparent slot of an embedded acrylic plate for a laser sheet to illuminate the region below the plate) divides the test section into two parts of equal cross-sectional area and serves as an intake lip for the defined inlet. This asymmetric design (with the 12° angled wedge in the top half of the channel), as shown in Fig. 1, is used to generate a relatively shock-free flow in the lower half, while it causes a series of oblique shock reflections in the upper half. Static pressure

traces are recorded on the bottom wall of the tunnel straddling a jet injection nozzle, using eight fast response (100 kHz) pressure sensors (S1–S8: PCB Piezotronics, Model 113A26). The sensors and the jet injection nozzle, placed between S4 and S5, are separated by 15 mm along the centerline of the bottom wall parallel to the freestream flow direction: S1 and S8 are located 60 mm upstream and downstream from the nozzle, respectively. The distance between the tip of the splitter plate (270 mm downstream from the converging/diverging nozzle throat) and the jet nozzle is 75 mm.

In the base configuration (Case I) shown in Fig. 1, the jet (ID = 3 mm) is injected through a relatively thick boundary layer (which originated upstream near the throat of the tunnel) into the flow through the model inlet defined in the lower half of the tunnel. The boundary layer on the upper wall of this inlet (i.e.. on the splitter plate) grows naturally from the leading edge of the plate. Four other inlet configurations are studied in this paper. All five of the configurations are summarized in Fig. 2, which also depicts the flow regions imaged by planar Rayleigh scattering (indicated qualitatively by the rectangles defined by the dashed lines).

In each case, the inlet channel height is fixed at 18.5 mm. As in Case I, Case II (Fig. 2a) has the splitter plate dividing the tunnel into upper/lower halves, but the wedged leading edge provides a series of shock/expansion reflections into the upper half region. In Case II, the jet is injected into the model inlet defined in this upper half through the splitter plate with the jet fluid delivered via a tube that traverses the lower half of the tunnel. This condition (Case II) has two important distinctions from Case I. First, the jet is now injected through a boundary later that originates from the splitter plate leading edge. This boundary layer is expected to be thin (and initially laminar) in comparison with that of Case I. Second, the inlet flow in Case II has a wedged wall, leading to flow compression and the formation of a series of moderately strong shock reflections. Cases III and IV (Fig. 2b) introduce a second splitter plate, with the two plates now fully isolating the inlet flow from the tunnel boundary layers. The two plates are separated by the same distance (18.5 cm) as that between the single plate and tunnel wall in Cases I and II. For Case III, both boundary layers grow naturally from the leading edge of the top and bottom splitter plate. For Case IV, sandpaper (100 grade) is applied between 0.5 and 2.5 cm (spanning the entire 4 cm width) from the splitter leading edge to trip the boundary layer to become initially turbulent. In Case V, the splitter plate is flipped along the vertical direction to provide an otherwise identical flow to Case II with a series of moderately strong shock reflections, but with one major distinction in that the jet is injected through a thick turbulent boundary layer, as in Case I.

Rayleigh scattering is carried out with a Nd:YAG laser (New Wave, Gemini PIV) capable of generating approximately 100 mJ/pulse (532 nm wavelength) with 10 Hz pulse repetition. The laser beam is transformed into a thin sheet of 0.5 mm thickness using a combination of two concave cylindrical lenses (200 mm focal length) and a convex spherical lens (250 mm focal length). The laser sheet spans a plane along the center line of the tunnel parallel to the freestream direction. Light scattered along a direction normal to the laser sheet is captured by an unintensified CCD camera (La Vision, Imager Intense, 1,376 by 1,040 pixel array) instrumented with a 50-mm Nikon lens. CO_2 fog (solid particles) produced in the nozzle scatters laser light and evaporates under varying environments provided by primary flow features such as shockwaves and boundary layers, where the local static temperature/pressure increases. Figure 3a shows the CO_2 sublimation curve as well as an isentropic expansion curve of the tunnel flow through the diverging nozzle. It is apparent that during the expansion process, the freestream flow crosses the sublimation curve of CO_2 at a Mach number of approximately Ma = 1.7. CO_2 particles, typically 10 nm in size (Miles and Lempert 1997), form and populate the freestream, in general, in proportion to the gas density. A typical Planar Laser Rayleigh Scattering (PLRS) image is presented in Fig. 3b taken in the absence of the jet for Case I. Note that there is an inaccessible region in the tunnel (white vertical bar), and this figure is a concatenation of two separate PLRS images. Shockwaves, boundary layers, and turbulent flow structures are well illustrated in the two-dimensional image illuminated by the planar laser light.

Laser firing for the PLRS is synchronized with the CCD camera exposure (3 μs shutter), as illustrated in Fig. 4. One of the laser pulses is selected to trigger the jet injection

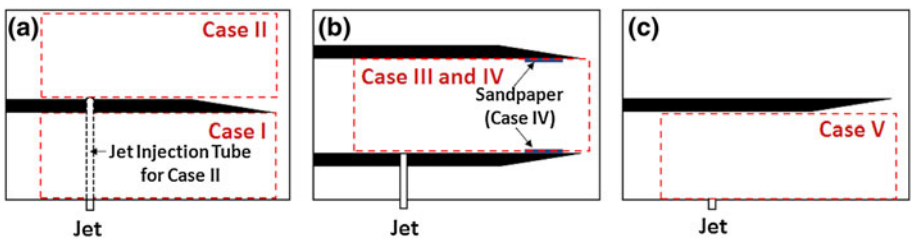

Fig. 2 The region of interest in each case (Case I through Case V) and configurations of the splitter plates

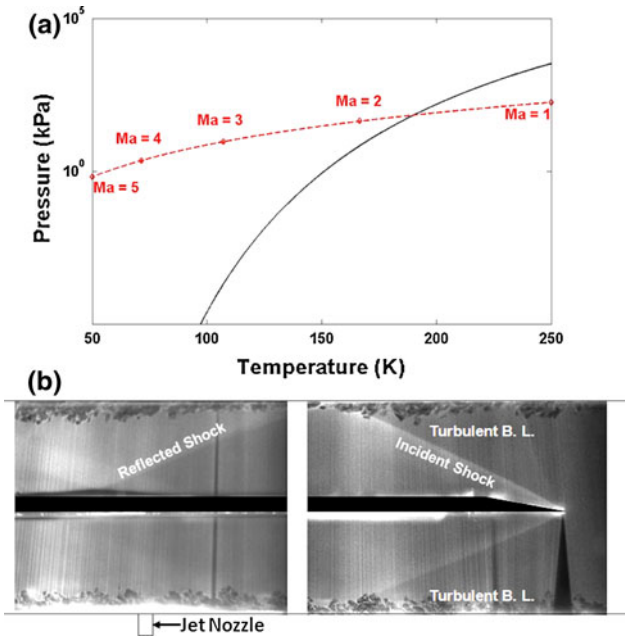

Fig. 3 **a** A carbon dioxide sublimation curve crossing isentropic flow condition curve in the Mach 5 tunnel and **b** a typical PLRS image of the tunnel flow with a splitter plate

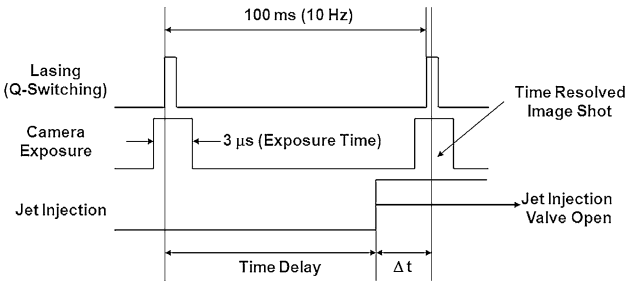

Fig. 4 A signal time table for taking a PLRS image at Δt after the jet injection valve opening signal

module while the tunnel is operating, but delayed as desired by a pulse delay generator (SRS, DG 535) to take time-synchronized images at different phases (Δt following the injection of the jet) in the flow evolution. The jet injection is controlled by a solenoid valve (ASCO, Red Hat II) driven by a controller (Optimal Engineering System Inc.) receiving its trigger signal from the delay generator. A sonic jet (air, in these studies presented here) is injected into the test section through a 3-mm diameter hole in the bottom wall resulting in a flow disturbance and an overall increase in flow pressure and temperature. Relevant to the jet interaction and mixing with the supersonic freestream is the square root ratio of the jet momentum flux to that of the freestream, defined by:

$$R = \sqrt{\frac{(\rho u^2)_{jet}}{(\rho u^2)_{\infty}}} = \sqrt{\frac{(\gamma p M^2)_{jet}}{(\gamma p M^2)_{\infty}}}$$

Here, ρ, u, γ, p, and M are gas density, velocity, ratio of specific heats, pressure, and Mach number of the jet (subscript *jet*) and freestream (subscript ∞) flow, respectively. The parameter, R, characterizes the penetration depth and mixing associated with the jet injection into a cross-flow (Smith and Mungal (1998)).

3 Results

3.1 Asymmetric wall boundary layer conditions

Here, we discuss the model inlet unstart dynamics induced by a jet injection with splitter configurations designated in Fig. 2, as Case I and Case II. These cases are referred to here as having *asymmetric* wall boundary conditions, in that they are primarily distinguished by the presence of either a thick turbulent boundary layer (Case I) or a thin laminar boundary layer (Case II) on the inlet wall through which the jet is injected. Another distinction (discussed later, when comparing Case I with Case V) is the presence of a moderately strong train of shock reflections due to the wedged inlet wall for Case II. Under the current flow condition, the model inlet is found to unstart 20 ± 0.5 ms and 25 ± 0.5 ms after the jet is triggered, for Case I and Case II, respectively.

Numerous studies have shown that the unstart shock is a critical flow feature in understanding the transient unstart phenomenon (Wieting 1976; Rodi et al. 1996; Wagner et al. 2008, 2009a, b; Do et al. 2010). As discussed later, a comparison of Cases I and II provides evidence for the significant role played by the presence of a turbulent boundary layer in prompting the formation of the unstart shock. The time sequential PLRS images in Figs. 5 and 6 illustrates the evolution of the flow features, while the flow undergoes unstart induced by a jet of $R = 4.5$. The entire flow region of interest (designated by the dashed rectangular region in Fig. 2) is interrogated in two separate Rayleigh scattering frames. The first frame illuminates the region in the vicinity of the jet nozzle (Fig. 5) and the other an upstream region near the tip of the splitter plate (Fig. 6). Each imaging region covers a 5 cm width along the freestream flow direction (from right to the left) and an 18.5 mm height. When combined, these two frames span the region within the dashed rectangular lines for Case I or Case II, in Fig. 2a.

The unstart process with the base configuration (Case I), as described in detail in a previous paper (Do et al. 2010), is discussed briefly here again and depicted in Figs. 5a and 6a. The figures reveal that the boundary layer growth/separation on the bottom wall of the inlet (also the bottom wall of the tunnel), initiated by the jet injection, propagates upstream (seen between 13 ms (Fig. 5a) and 17 ms

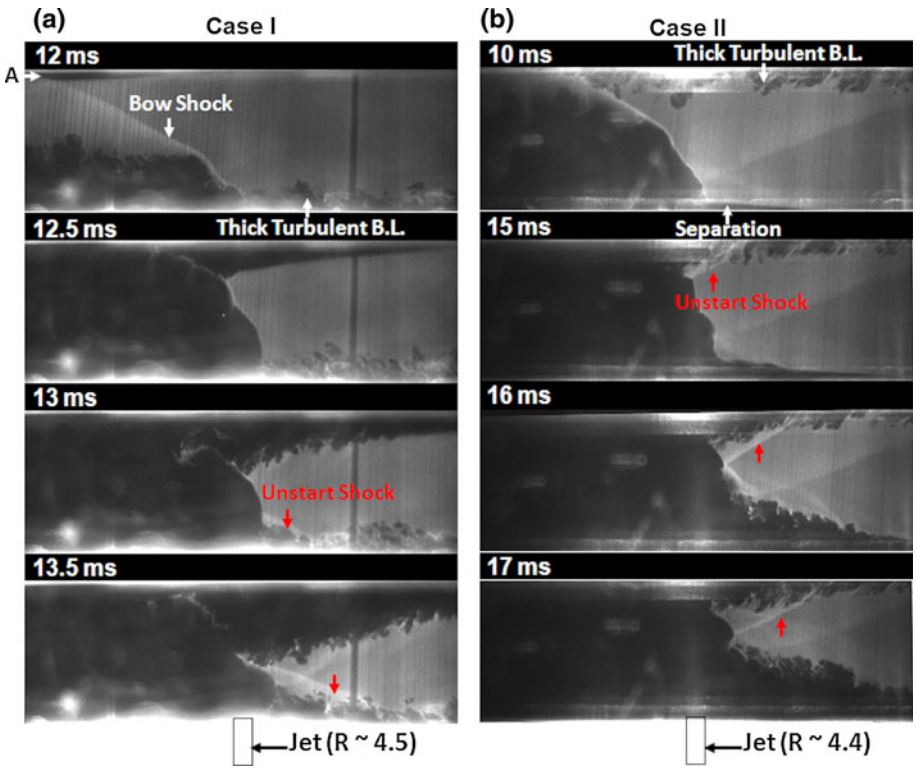

Fig. 5 Time sequential PLRS images taken in the adjacent to the jet with the configurations of **a** Case I and **b** Case II

(Fig. 6a) after jet triggering) and produces an oblique unstart shock first appearing in front of the jet in the 13-ms panel of Fig. 5a. The shock emerging at 13 ms on the bottom wall in Fig. 5a is referred to as the "unstart shock" because the flow unstarts upon the arrival of this shock at the tip of the model inlet. The unstart shock leading the separation region on the bottom surface is qualitatively similar to that shown by Wagner et al. (2009a, b) with asymmetric wall boundary conditions that precede a complex unstart shock system. This shock propagates forward, and the inlet flow unstarts shortly after the arrival of this shock at the inlet (Fig. 6a, 17 ms). Concurrently, we also see a separated flow on the upper wall (Fig. 5a, 12 ms) when the jet-induced bow shock interacts with this thin boundary layer (A in Fig. 5a). This upper wall disturbance also propagates upstream, preceding the unstart shock, and arrives at the tip of the splitter plate at 13.5 ms (Fig. 6a). It is trailed by a rapidly growing boundary layer that appears to become turbulent within one inlet duct height downstream distance (B in Fig. 6a).

Several flow structures, such as the formation and evolution of the unstart shock, separated flow regions and developing boundary layers seen for Case II (Figs. 5b, 6b) appear to be very similar to those seen in Case I (Figs. 5a, 6a), particularly apparent if the images of Case II are flipped vertically. Shortly following the injection, we see the emergence of a separated flow just upstream of the jet on the initially thin laminar boundary layer (first emerging on the bottom at 10 ms as indicated in Fig. 5b). As in Case I, this separated flow appears to propagate upstream and is followed by the growth of a thick turbulent boundary layer/separated flow, reaching the wedged region of the splitter tip at 20 ms (Fig. 6b). Surprisingly, the unstart shock is spawned on the opposite surface at a time of about 15 ms (Fig. 5b) and moves upstream between 15 ms (Fig. 5b) and 24.5 ms (Fig. 6b), along the surface. Here, it is noteworthy that, in both Cases I and II, the unstart shock emerges on the surface where there is initially (prior to the jet injection) a thick turbulent boundary layer, suggesting that this thick turbulent boundary layer prompts the formation of this oblique unstart shock. Note that qualitatively, the same flow features appear, albeit at different times in each case, e.g., the unstart shock emerges at 13 ms in Case I (Fig. 5a) and 15 ms in Case II (Fig. 5b). This 2-ms difference may be attributed to several factors, but most likely due to the longer jet gas delivery tube in Case II (the estimated R in Case II is $\sim$ 4.4, when the upstream jet pressure is the same as that in Case I), the different wall boundary conditions where the jet is discharged (Case I is turbulent, Case II is laminar) and/or the pressure disturbances caused by incident shocks, presumably stronger in Case II with the wedged intake lip.

3.2 Symmetric wall boundary conditions

We have seen in Sect. 3.1 that while wall boundary conditions (asymmetric, i.e., one wall turbulent, the other

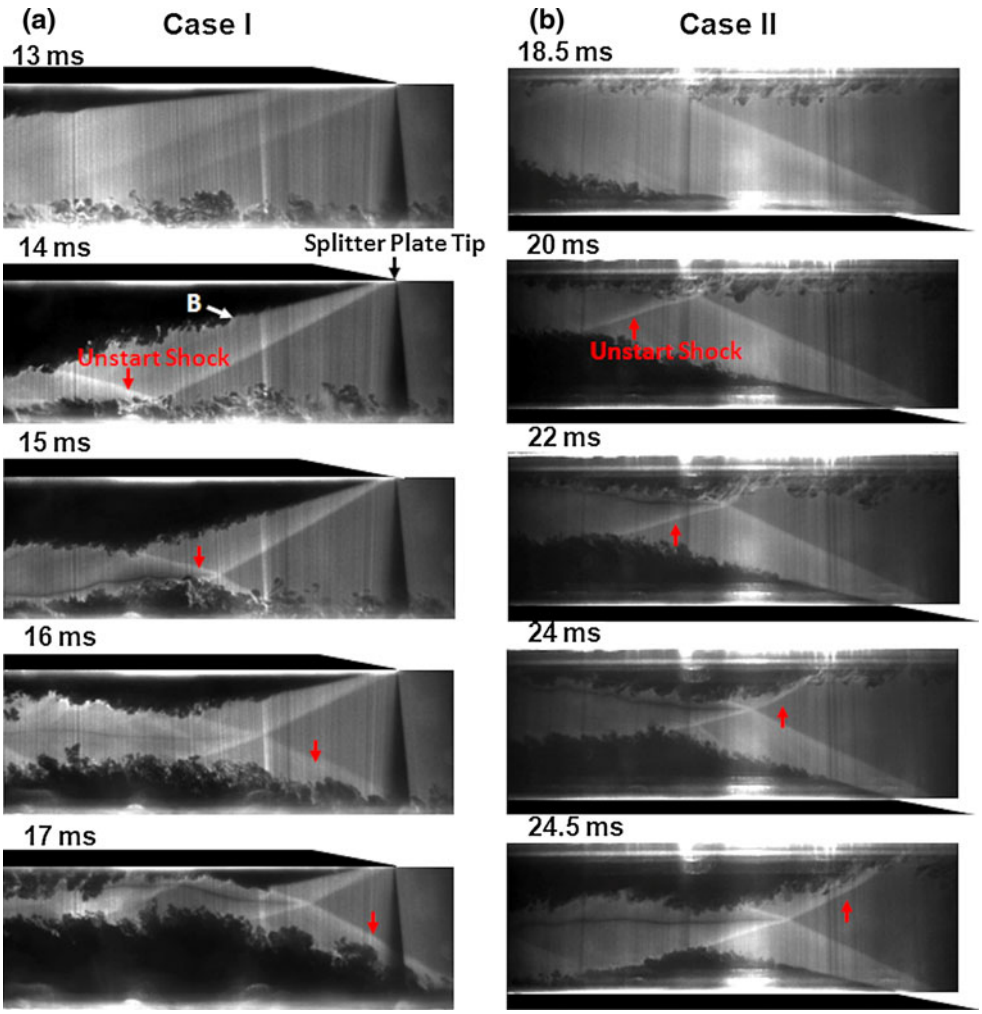

Fig. 6 Time sequential PLRS images covering the first 5-cm region downstream of the splitter tip taken with the configurations of **a** Case I and **b** Case II

laminar) affect the transient unstart flow features, injecting through either a turbulent or laminar boundary layer is not found to cause significant differences in the overall time to unstart the inlet flow. In the section, we describe the *symmetric* inlet flow studies, Cases III and IV (Fig. 2b), which provide the same wall boundary conditions on the top and bottom walls of the model inlet flow. For Case III, both boundary layers are thin and initially laminar, while in Case IV, both walls have relatively thick turbulent boundary layers prior to jet injection.

We find that with the Case III configuration, the oblique unstart shock that was seen to emerge in Cases I and II *does not appear*, and the time required for complete inlet unstart is significantly longer in comparison with the time measured for the other cases. Figure 7 presents the Rayleigh scattering images for the two frames spanning the entire region of interest, depicting the inlet flow observed for Case III over a time ranging from prior to jet injection through to flow unstart, at a time of 55 ms after jet triggering. As shown in Fig. 7a (taken in the absence of the jet), the two splitter plates (with wedge outward facing) isolate the main flow from the turbulent boundary layers on the tunnel walls to define the model inlet. In this configuration, thin (initially laminar) boundary layers form on both upper and lower walls. Weak shock waves appear originating from the splitter tips, most likely due to the small but finite dimensions of the tips. Note that the interaction of the shock originating from the lower wall induces flow separation on the upper wall (C in Fig. 7a), at a downstream location of approximately 40 mm. The flow is seen to undergo a laminar to turbulent flow transition, with the clear indication of relatively thin turbulent boundary layers in the downstream frame. Figure 7b is a similar depiction, taken shortly after jet injection (approximately 17 ms after jet triggering). At this time, we see from the brighter region that spans across the inlet at approximately 20 mm upstream of the jet, which a compression wave (presumably leading a pseudo-shock structure) forms, almost normal to the flow direction, as indicated by the diffuse, brighter signal at the center of the channel. This compression is followed by the apparent thickening of the turbulent boundary layers on both top and bottom surfaces.

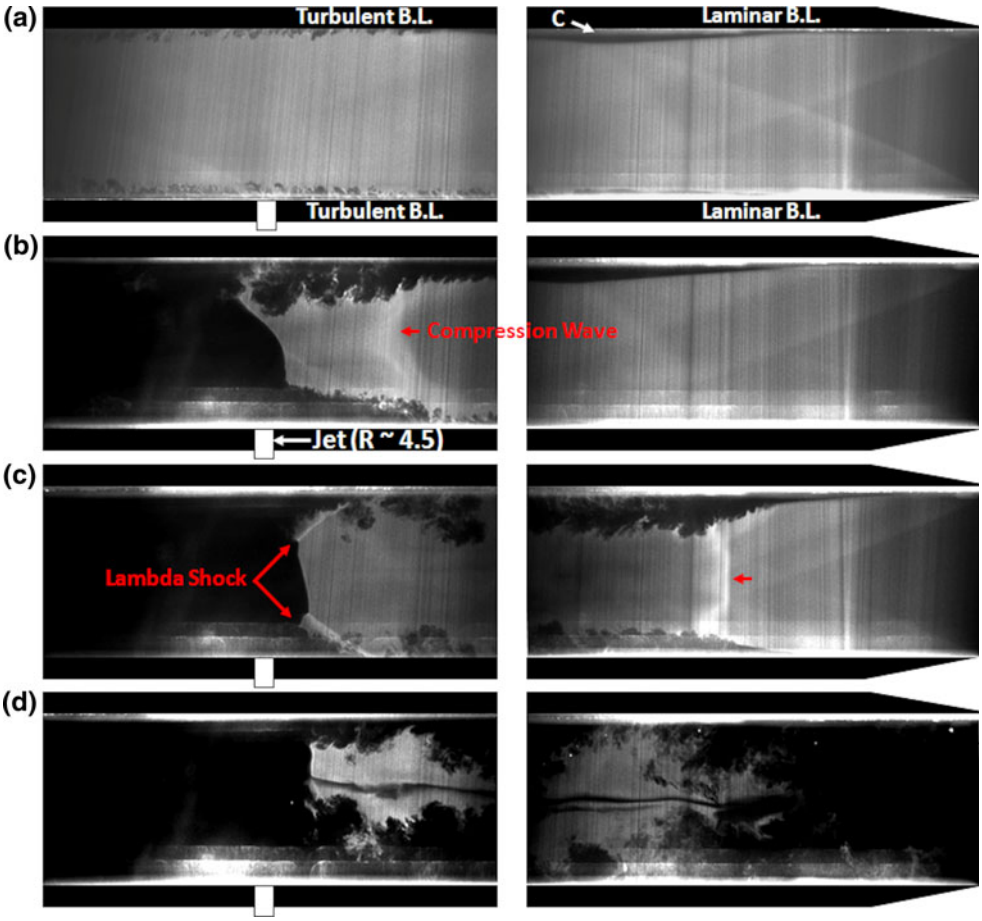

Fig. 7 PLRS images with Case III configuration: **a** before the jet injection **b** the formation of a compression wave (16–17 ms after the jet injection), **c** a dual-shock structure (an upstream pseudo-shock and a downstream shockwave) seen in the time duration of 18–55 ms, and **d** breakdown of the dual-shock structure at 55 ms

This compression wave propagates upstream and arrives at a position of about 27 mm from the splitter tip within about 1 ms (see Fig. 7c) remaining there for approximately 37 ms (from 18 to 55 ms). This compression wave is thicker than typical shockwaves such as the oblique unstart shock seen in Cases I and II or the incident shocks originating from the splitter tips and is not strong enough to cause transition to subsonic flow. This is evident from the fact that we still see significant Rayleigh scattering off of CO_2 fog behind this wave, as this fog would be expected to evaporate in subsonic flow regions (Fig. 3a). In addition, we see from Fig. 7c what appears to be a normal shock (little can be said about this with the present diagnostic) and the emergence of a lambda shock downstream of this compression wave, just upstream of the jet.

So-called pseudo-shocks are often observed in internal flows in the presence of wall friction through a duct of constant cross-sectional area (Hataue 1989; Arai et al. 1990; Matsuo et al. 1999; Katanoda et al. 2003) and seem to accompany the growth of turbulent boundary layers when a supersonic flow decelerates to a subsonic flow in a duct. Therefore, one can expect its presence in the supersonic internal flows investigated here. We suppose that the pseudo-shock structure does not emerge in Cases I and II due to the presence of thick turbulent boundary layers in the flow channel (region of interest in Cases I and II). This thick turbulent boundary layer prompts the formation of the unstart shock earlier (13–15 ms in Cases I and II, Fig. 5) than the emergence of the pseudo-shock structure (16–17 ms in Cases III and IV, Figs. 7 and 9) and would inhibit the evolution of the pseudo-shock. Arai et al. (1990) observed experimentally that a series of shocks (compression waves) in the pseudo-shock region intermittently pressurize and decelerate a supersonic flow in a square duct, and boundary layers were found to thicken abruptly behind the first compression wave, in ways consistent with what we observed here in Fig. 7b and c. In numerical simulations, Hataue (1989) predicted a flow structure in a duct (Ma = 3) that consisted of an upstream compression wave leading a pseudo-shock region together with a downstream shock that produced a subsonic flow. The downstream shock was strongly deformed by the interaction with the now thickened boundary layers. This "dual-shock" (pseudo-shock region) structure appears to be qualitatively similar to that shown in Fig. 7c. It is noteworthy that our flow Mach number (Ma $\sim$ 5) is significantly higher than Ma = 3. Matsuo et al. (1999) claimed that the shocks in the pseudo-shock region would be

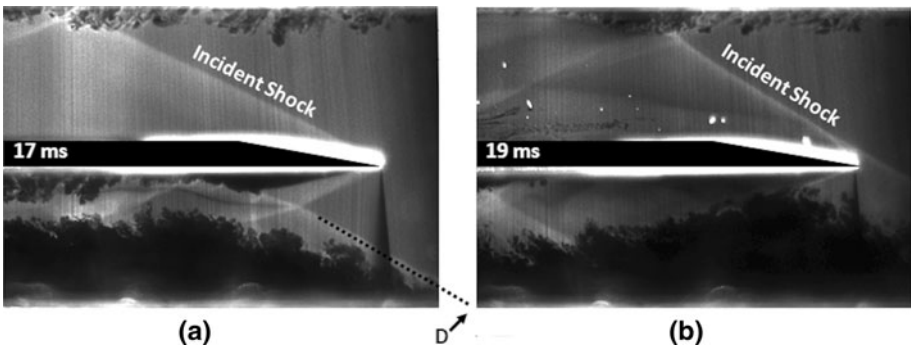

Fig. 8 PLRS images revealing that the unstart shock propagates further upstream out of the imaging region in Case I

oblique in the high Mach number condition. However, our flow condition is distinguished from that of other studies investigating pseudo-shock structure by the fact that the supersonic internal flow decelerates primarily due to a downstream pressure rise induced by downstream jet injection. Therefore, the flow deceleration should be faster than that purely by wall friction and boundary layer development, which may alter the angle of the compression wave leading the pseudo-shock region.

A sudden breakdown of this dual-shock structure leading to inlet flow unstart is observed (see Fig. 7d) at a time of 55 ms ± 0.5 ms. The breakdown occurs swiftly, within 1 ms. It is noteworthy that, in Case III, it therefore takes about 55 ms for the inlet flow to unstart—a time that is significantly longer than that of the previous two cases discussed (20 ms (Case I) and 25 ms (Case II)). Inlet unstart appears to be delayed by the isolating of inlet flow from the thick turbulent boundary layer on the tunnel walls. At this time, however, the physics related to the sudden breakdown of the flow structure is not resolved. We believe that this breakdown is caused by the relatively slow buildup in pressure behind the upstream pseudo-shock or pressure disturbances from the downstream region. This flow breakdown mechanism will be examined in future studies in which pressure measurements will be taken along the inlet walls of the isolated flow.

From the observations made with the Case III configuration, it appears that preexisting thick turbulent boundary layers on the tunnel wall prompt the formation of the unstart shock seen in the Cases I and II configurations. In the Case I and II studies, this thick turbulent boundary layer is a nascent feature of the tunnel flow, growing along the tunnel wall (which serves as one wall defining the inlet) and originating in the throat region of the converging–diverging nozzle, far upstream of the splitter tip. This thick boundary layer provides a subsonic region that can possibly channel the propagation of downstream flow (e.g., pressure) disturbances into the region upstream of the splitter tip. For example, the unstart shock in Case I can propagate far upstream beyond the splitter plate edge, as shown in Fig. 8. The foot of the unstart shock (D in Fig. 8a) on the bottom wall is beyond the image field in the 17-ms panel (Fig. 8a) and continues to propagate further upstream at 19 ms (Fig. 8b), where it now disturbs the flow in the upper half of the tunnel, reducing the Mach number as confirmed by the increase in the incident shock angle (Fig. 8b). This makes a direct comparison of the later stages of unstart in Case III with Cases I and II difficult, because, as shown in Fig. 8, the turbulent boundary layer on the tunnel walls (in Cases I and II) results in an unstart shock that disrupts the upstream flow region before the complete unstart of the inlet flow—a situation not encountered in Case III.

Case IV (same geometrical configuration of Case III) also isolates the inlet from this thick turbulent boundary layer, but generates its own relatively thick turbulent wall boundary layers by the use of sandpaper near the leading edge of the splitter isolator plates. Figure 9a reveals the presence of turbulent boundary layers developing on the splitter plates generated by sandpaper attached 5 mm downstream of the plate tips. An earlier complete inlet unstart (25 ms) compared with that seen in Case III (55 ms) is observed with this configuration. This unstart is about as fast as that seen in Cases I (20 ms) and II (25 ms), although the general flow features are more similar to those seen for Case III. A pseudo-shock structure emerges behind the intersection of the two incident shocks accompanying the development of thick turbulent boundary layers and anchoring at a quasi-stable position for 8 ms (16–24 ms after jet triggering), as seen in Fig. 9b. Then, a sudden break down of this flow structure (dual-shock) is observed at 25 ms (Fig. 9c) instantly followed by complete inlet unstart. We attribute this early unstart, in comparison with that of Case III, to the initial turbulent boundary layers on the upper and lower inlet walls.

3.3 The effect of jet momentum flux and incident shock

The boundary layer separation seen in the unstart process is initiated by the downstream pressure rise accompanying the jet injection, generating an adverse pressure gradient on the surfaces (tunnel walls and splitter plates). This pressure

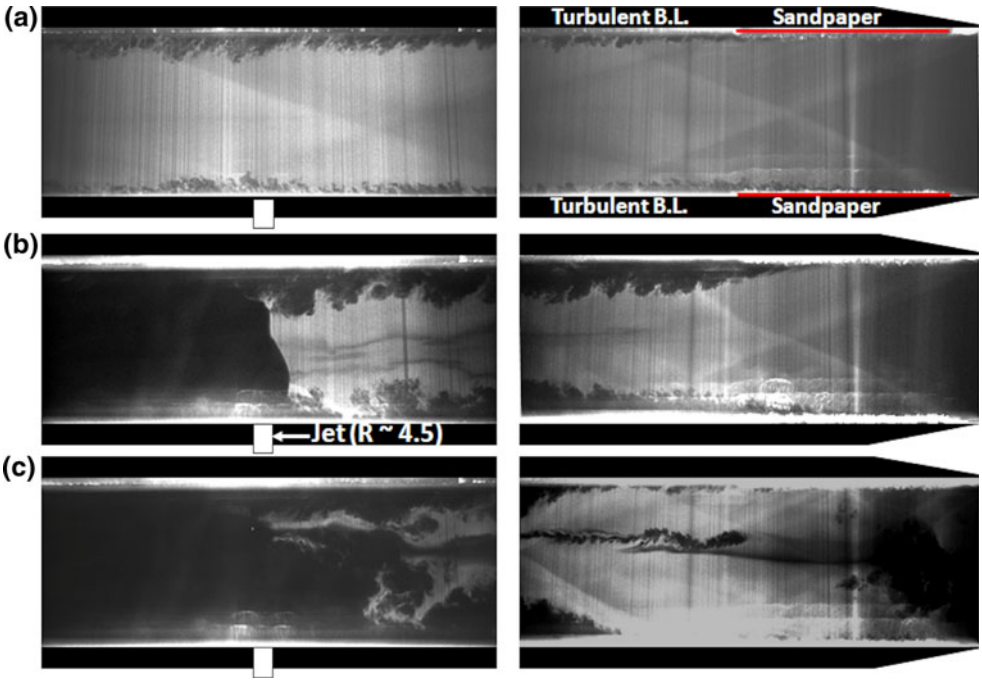

Fig. 9 PLRS images with Case IV configuration: **a** before the jet injection, **b** shockwaves intersecting each other at the inlet and standing steady during 16–24 ms, and **c** tunnel unstart at 25 ms

Table 1 Jet pressure conditions

R	Jet stagnation pressure	Jet exit static pressure (kPa)
3.5	540	280
3.7	620	330
3.9	690	360
4.1	770	410
4.3	840	450
4.5	900	480

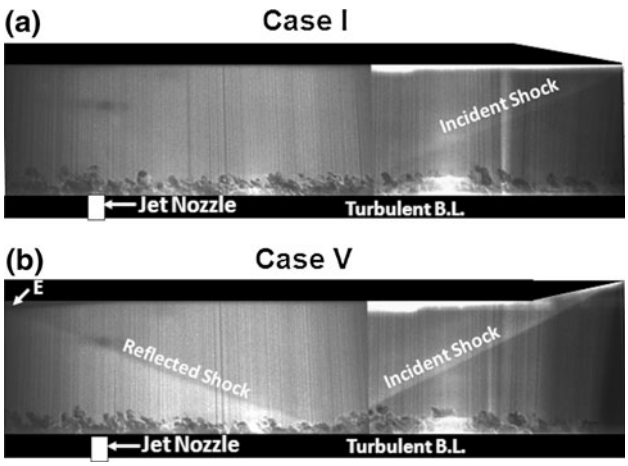

Fig. 10 PLRS images depicting **a** a weak incident shock in Case I and **b** relatively strong incident shock in Case V

gradient is primarily regulated by the amount of mass injection via the jet (depending on the square root ratio of the jet momentum flux to that of the freestream (R)) and the surface pressure distribution measured by the pressure sensors is influenced by shock/expansion impingements and reflections on the surface (e.g., incident shockwave originating from the tip of splitter plate). Here, we describe the effects of varying R and of the incident shockwaves on the boundary layer separation and/or downstream pressure rise by comparing Case I with Case V, the latter providing a stronger incident series of shock reflections in the inlet flow.

The jet conditions are given in Table 1. Jet stagnation pressure at the nozzle exit is estimated from the Ashkenas–Sherman correlation (Ashkenas and Sherman 1965) with the location of the Mach disk measured by Schlieren imaging. The static pressure at the jet nozzle exit is calculated assuming isentropic sonic jet expansion.

Figure 10 shows concatenated PLRS images (a mosaic of two images spanning the region near the splitter tip to that near the jet nozzle, from independent runs) of the flow for Cases I and V, in the absence of jet injection. The weak (smaller shock angle by 3° in comparison with that of Case V) oblique shock in Case I (Fig. 10a) arises due to the finite thickness of the tip and/or slight misalignment of the splitter plate surface relative to the direction of the main flow. This oblique shock in Case I shows no significant evidence of reflection from the lower wall. The stronger shock in Case V (Fig. 10b) is due to the presence of the wedged leading edge, and a reflection from the thick turbulent boundary layer is clearly visible. While no boundary layers (presumed laminar over this region imaged) are resolved on the upper wall (surface of the splitter plate), some evidence is apparent of a thickening of this boundary

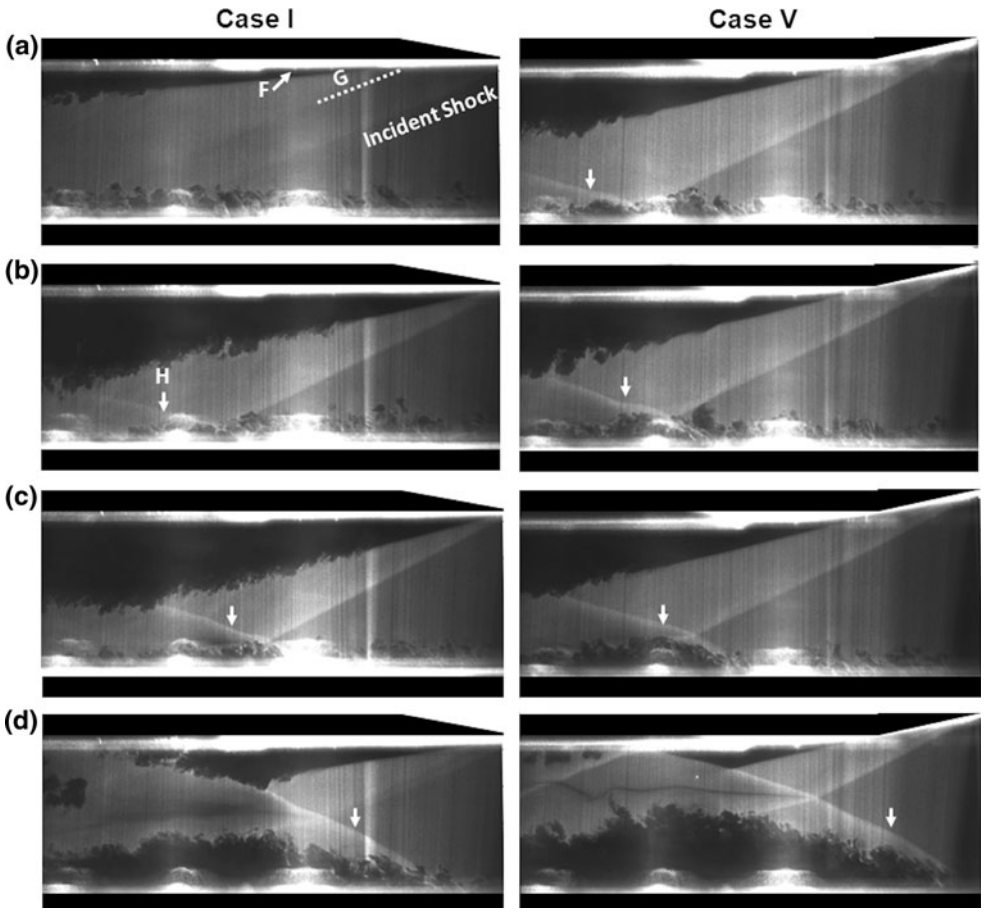

Fig. 11 PLRS images taken with increasing R in Cases I and V: $R \sim$ **a** 3.5, **b** 3.7, **c** 3.9 and **d** 4.1. These flow structures are steady during the jet injection time period ($\sim$1 s)

layer due to separation where the Case V reflected shock impinges on the upper wall (E in Fig. 10b). We note here that while the turbulent boundary layer edge and its detailed structure appears to be clearly visible on the lower wall, covering approximately 25% of the channel height, an interpretation of what this PLRS image demarcation represents is still only qualitative at best, as it represents that region of the flow where the CO_2 fog sublimes, near temperatures of about 200 K, due to boundary layer heating.

The images in Fig. 11 cover the first 5 cm of the flow downstream of the splitter tip. Images (a) through (d) reflect an increase in R, from 3.5 to 4.1, in 0.2 intervals. Under these lower R conditions, the primary flow features, including shockwaves and boundary layers, appear to be "quasi-steady" between 20 ms (following jet triggering) until the jet is deactivated approximately 1 s later. An interesting observation here is that the flow evolution with increasing R is exactly the same as that seen in Fig. 6a, which is the temporal evolution of the flow undergoing unstart with the jet of $R \sim 4.5$, while the model inlet never unstarts when R is lower than 4.3, i.e., some portion of the flow within the test section remains supersonic. This further confirms the sequence of the unstart events seen in Fig. 6a. Note also that for the present configuration, $R = 4.3$ corresponds to 0.01 kg/s mass injection via the jet into 0.03 kg/s mass flow through the channel (half of the tunnel). At the lowest R (Fig. 11a, Case I), the major flow disturbance seen in this imaging region is that of the boundary layer growth on the splitter plate, originating from what is presumed to be a separation in the flow, and its wedge-like forefront (F in Fig. 11a Case I) spawns a weak shockwave (G in Fig. 11a Case I) seen just downstream of the weak shock emanating from the splitter plate tip. This quasi-steady flow structure appears to be the same as that observed at an early stage of the unstart process for higher R, as shown in the 13-ms panel of Fig. 6a. Also, the flow structures of (b) through (d) appear similar to those in the 14-ms through 16-ms panels of Fig. 6a. As R increases, a shockwave (H in Fig. 11b Case I) appears on the bottom wall induced by the separation of the turbulent boundary layer, and this standing shockwave advances upstream with higher R (Fig. 11b, c and d, Case I). Based on this observation, the temporal evolution of the unstart, such as that seen in Fig. 6a, can be described as a series of events starting with a pressure buildup downstream of the jet, leading to flow separation on internal walls of the inlet, in some cases, accompanied the formation of the unstart

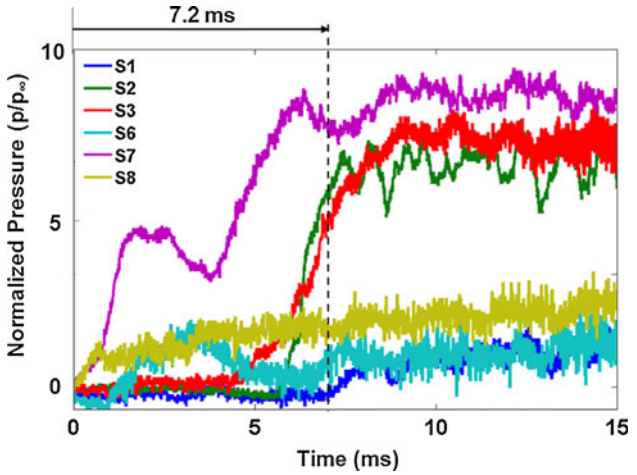

Fig. 12 Pressure traces (normalized by freestream pressure (p_∞)) recorded on the *bottom surface* of the tunnel with the jet of $R \sim 3.9$ in Case I. The arrival time of the pressure rise at S1 relative to the first pressure rise at S8 is indicated, 7.2 ms

shock. The variation in the shock position with changing R is also apparent in Case V, although the shock has advanced further toward the upstream region in comparison with Case I.

The downstream pressure rise induced by the air jet injection is clearly evident in the recorded pressure traces. Figure 12 documents the sudden pressure rise at the various locations for $R = 3.9$ and for the Case I configuration. The reference time ($t = 0$ s) in the figure corresponds to the initial pressure rise at the sensor located at S8 (i.e., the farthest downstream region characterized). The pressure at S8 rises abruptly at approximately 10 ms after triggering of the jet. Absolute pressure offsets are subtracted from the traces to highlight relative differences between the pressure recorded before and after the jet injection. The pressure traces recorded at the locations nearest to the jet nozzle (S4 and S5, not shown) fluctuate significantly, due to flow instabilities in the near field of the jet. It is apparent that the pressure disturbance propagates toward the upstream region of the tunnel, presumably along the subsonic boundary layer, in succession through to the location at S1. This transient pressure response confirms that the high pressure disturbance, initiated far downstream of the jet provides an adverse pressure gradient that can result in flow separation. The time required for the propagation of the pressure disturbance from S8 to S1 (over a 12 cm distance) is 7.2 ms, corresponding to a speed of 17 m/s (2.5% of freestream speed).

We find that the speed of propagation of this pressure wave increases with increasing R, as seen in the graphs of Figs. 13 and 14. The time of arrival for the rise in pressure at the locations of S1–S3 and S6 is plotted as a function of R (from 3.5 to 4.3) for both Cases I (Fig. 13a) and V (Fig. 13b). The arrival time at S1–S3 decreases significantly as R increases, while it exhibits a much weaker dependence on R at S6. The reason for this behavior is that the flow disturbance in the wake of the jet (e.g., at S6) occurs directly from the increase in mass flow rate in the inlet leading to pressure/temperature elevations in the flow, in contrast with the upstream region (e.g., at S1–S3) where the boundary layer growth/separation depends on the upstream propagation of this pressure rises. We also note that for Case I, the high pressure region propagates upstream and crosses S1 when R is greater than 3.9, while it seems to remain anchored behind S2 when R is 3.5. This result is consistent with the features seen in Fig. 11 (Case I).

The arrival times for the pressure disturbances for Case V (when there is a relatively strong initial oblique shock) are notably different (Fig. 13b). As seen for Case I, it appears that the arrival time at S6 is not strongly influenced by variations in R, whereas the arrival time decreases strongly at the other locations when R increases. However, it is apparent that the difference in the arrival time as recorded between S6 to S3 is longer for Case V than Case I, indicating that the disturbance propagates at slower speed in this downstream region, when there is a relatively strong shock reflection near the location of S3. The speed estimated from the transit time between the two sensors is plotted as a function of R for both configurations in Fig. 14. With the exception of the lowest value of R studied, the case of a strong shock reflection (Case V) at S3 results in lower propagation speed.

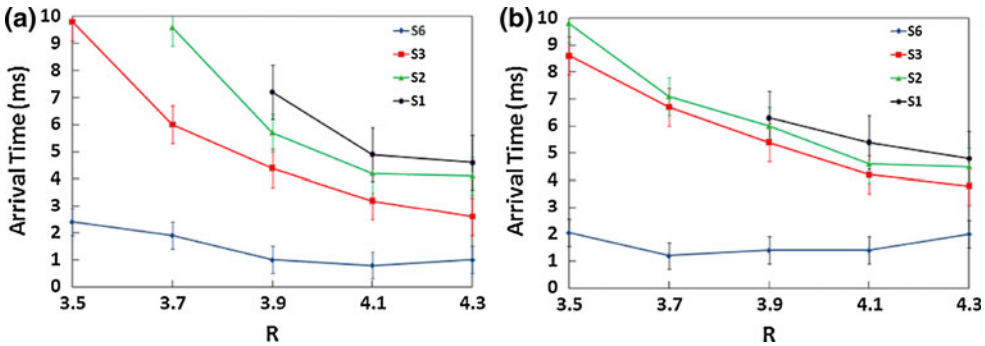

Fig. 13 The arrival times of pressure rise at the locations of pressure sensor (S1, S2, S3, and S6) are plotted as a function of R **a** Case I and **b** Case V

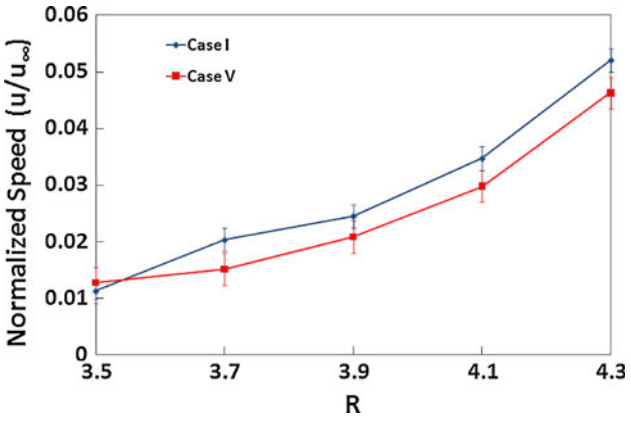

Fig. 14 A plot of high pressure region propagation speed (normalized by freestream flow velocity (u_∞)) between S6 and S3 as a function R

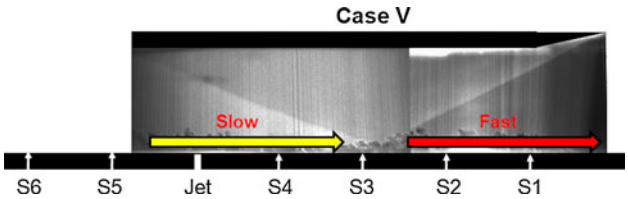

Fig. 15 A PLRS image with a summary of the effect of a relatively strong incident shock (Case V) in comparison with that of Case I

Figure 15 illustrates the effect of the incident shock on the propagation of the high pressure region. The effect of the strong incident shock in Case V appears in two different ways on the surface, downstream (slower propagation of the high pressure region) and upstream (faster propagation) of S3 where the incident shock is reflected as shown in Fig. 15. We believe that the shock reflection in the region adjacent to S3 provides a locally favorable pressure gradient, delaying the pressure rise in the downstream region. In Case V, the pressures at S3 and S4 are approximately 5 and 3.5 kPa higher than those in Case I in the absence of the jet, respectively. Therefore, a greater downstream pressure buildup is required to overcome this local favorable pressure gradient for further propagation. The shock reflection near S3 accelerates the propagation in the upstream region (between S3 and S1). The propagation speeds between S3 and S1 are approximately 15 m/s in Case I and 30 m/s in Case V in a range of R between 3.9 and 4.3.

4 Summary

An in-draft Mach 5 wind tunnel was used to generate approach flow conditions for studies of unstart in model inlets. In the studies described, inlet unstart is generated by the injection of an air jet. Flow dynamics following jet injection were investigated with five different inlet configurations and varying jet injection momentum.

Planar Laser Rayleigh Scattering imaging was used to characterize flow features, including the evolution of boundary layers and shocks. We find that unstart flow features and the overall inlet unstart process are strongly affected by the characteristics of the initial wall boundary layer prior to jet injection. In asymmetric inlet configurations, with a thick turbulent boundary layer on one wall and a thin (initially laminar) boundary layer on the other, an unstart shock emerges, but only on the wall with an initially thick turbulent boundary layer, independent of the boundary layer through which the jet is injected. In either case, complete unstart of the inlet occurs within about 25 ms. With symmetric wall configurations (i.e., cases in which wall boundary layers are similar on both sides, either turbulent or laminar), there is no oblique unstart shock. Instead, we see a relatively weak compression wave or pseudo-shock, which initially propagates upstream in advance of unstart and remains quasi-stable for some time, until a catastrophic breakdown in the structure occurs and the inlet flow unstarts completely. The duration over which this pseudo-shock is anchored in the inlet depends on the nature of the initial boundary layer (thin laminar or thick turbulent). With relatively thin (initially laminar) boundary layers, the pseudo-shock appears stable until 55 ms following jet injection—more than twice as long as the case in which the initial boundary layers are tripped to be turbulent (25 ms). The time for unstart in the turbulent symmetric condition is comparable with that of the asymmetric cases.

These results suggests that inlet unstart can be effectively delayed or avoided by the control of boundary layers on inlet walls as reported by Kodera et al. (2003) and Valdivia et al. (2009). Unstart is initiated by the boundary layer separation induced by adverse pressure gradients formed by downstream pressure elevations following jet injection. This has also been predicted in the numerical study by McRae and Neaves (1994). They found that laminar, viscous flow, unstart occurs by a separation/oblique shock mechanism rather than by a movement of a normal shock. Wall pressure measurements indicate that the speed of propagation of this pressure rise along the boundary layer increases with increased jet momentum. While jet injection at any value of R, the jet momentum ratio, disrupts the initial flow structure and initiates unstart, we find that there is a threshold value for R (= 4.3) for the complete unstart of the inlet during our facility flow time (several seconds), which corresponds to 0.01 kg/s mass injection into 0.03 kg/s mass flow through the channel (half of the tunnel). In an actual scramjet engine system, this inlet unstart threshold can be determined by fuel flow rate into the combustor (Curran and Murphy 2000). The

complete inlet unstart is confirmed by the PLRS image of no laser scattering signal from particulate CO_2 in the flow channel (region of interest in each case) sublimating under elevated temperature/pressure conditions when the flow unstarts and flow disturbances at the inlet in the region out of the channel, e.g., the upper half of the tunnel in Fig. 8, following jet injection.

Finally, asymmetric experiments with strong shock reflections indicate that shock impingement on the turbulent boundary layer, through which the pressure disturbance propagates, can produce local conditions that can strongly alter the propagation speed of the disturbance. Shock/turbulent-boundary layer interactions in inlet flows are expected, therefore, to strongly impact the unstart dynamics. This finding also suggests that other ways that can generate a local momentum flux perturbation, such as electric discharge boundary-layer actuation (Im et al. 2010), might be particularly useful in advanced unstart mitigation strategies.

Acknowledgments This work is sponsored by the Department of Energy sponsored Predictive Science Academic Alliance Program (PSAAP) at Stanford University.

References

Andreadis D (2004) Scramjet engines enabling the seamless integration of air & space operations. The Industrial Physicist, Aug/Sept 2004

Arai T, Sugiyama H, Abe F, Takahashi T, Onodera O (1990) Internal structure of pseudo-shock waves in a square duct. AIP Conf Proc 208:850–855

Ashkenas H, Sherman RS (1965) The structure and utilization of supersonic free jets in low density wind tunnels. Rarefied Gas Dyn 2:84–105

Curran ET, Murphy SNB (2000) Scramjet propulsion, progress in astronautics and aeronautics 189, AIAA Inc., USA: 183

Curran ET, Heiser WH, Pratt DT (1996) Fluid phenomena in scramjet combustion systems. Annu Rev Fluid Mech 28:323–360

Do H, Im S, Mungal MG, Cappelli MA (2010) Visualizing supersonic inlet duct unstart using planar laser Rayleigh scattering. Exp Fluids (accepted for publication) doi 10.1007/s00348-010-1028-4

Emami S, Trexler CA, Auslender AH, Weidner JP (1995) Experimental investigation of inlet-combustor isolators for a dual-mode scramjet at a Mach number of 4. NASA Technical Paper 3502

Graham RH (2002) SR-71 Blackbird. MBI Publishing Company, St. Paul, pp 27–28

Hataue I (1989) Computational study of the shock-wave/boundary-layer interaction in a duct. Fluid Dyn Res 5:217–234

Hawkins WR, Marquart EJ (1995) Two-dimensional generic inlet unstart detection at Mach 2.5–5.0. In: 6th international aerospace planes and hypersonics technologies conference, Chattanooga, TN, USA

Heiser WH, Pratt DT (1993) Hypersonic air breathing propulsion. In: AIAA education series, Washington, DC

Im S, Do H, Cappelli MA (2010) Dielectric barrier discharge control of a turbulent boundary layer in a supersonic flow. Appl Phys Lett 97:041503

Katanoda H, Matsuoka T, Matsuo K (2003) Experimental study on shock wave structures in constant-area passage of cold spray nozzle. J Thermal Sci 16:40–45

Kodera M, Tomioka S, Kanda T, Mitani T, Kobayashi K (2003) Mach 6 test of a scramjet engine with boundary-layer bleeding and two-staged fuel injection. In: 12th AIAA international space planes and hypersonic systems and technologies, Norfolk, VA, USA

Mashio S, Kurashina K, Bamba T, Okimoto S, Kaji S (2001) Unstart phenomenon due to thermal choke in scramjet module. In: AIAA/NAL-NASDA-ISAS 10th international space planes and hypersonic systems and technologies conference, Kyoto, Japan

Matsuo K, Miyazato Y, Kim H (1999) Shock train and pseudo-shock phenomena in internal gas flows. Prog Aerospace Sci 35:33–100

McDaniel KS, Edwards JR (2001) Three-dimensional simulation of thermal choking in a model scramjet combustor. In: 39th aerospace sciences meeting and exhibit, Reno, NV, USA

McRae DS, Neaves M (1994) Time accurate computation of unsteady hypersonic inlet flows with a dynamic flow adaptive mesh, Technical Report, AFRL-SR-BL-TR-98-0091

Miles RB, Lempert WR (1997) Quantitative flow visualization in unseeded flows. Annu Rev Fluid Mech 29:285–326

O'Byrne S, Doolan M, Olsen SR, Houwing AFP (2000) Analysis of transient thermal choking processes in a model scramjet engine. J Propulsion Power 16:808–814

Poggie J, Erbland PJ, Smits AJ, Miles RB (2004) Quantitative visualization of compressible turbulent shear flows using condensate-enhanced Rayleigh scattering. Exp Fluids 37:438–454

Rodi PE, Emami S, Trexler CA (1996) Unsteady pressure behavior in a ramjet/scramjet inlet. J Propulsion Power 12:486–493

Sato S, Izumikawa M, Tomioka S, Mitani T (1997) Scramjet engine test at Mach 6 flight Condition. In: 33rd AIAA/ASME/SAE/ASEE joint propulsion conference and exhibit, Seattle, WA, USA

Shimura T, Mitani T, Sakuranaka N, Izumikawa M (1998) Load oscillations caused by unstart of hypersonic wind tunnels and engines. J Propulsion Power 14:348–353

Smith SH, Mungal MG (1998) Mixing, structure and scaling of the jet in crossflow. J Fluid Mech 357:83–122

Tam C, Eklund D, Behdadnia R (2008) Influence of downstream boundary conditions on scramjet-isolator simulations. In: 26th AIAA applied aerodynamics conference, Honolulu, HI, USA

Valdivia A, Yuceil KB, Wagner JL, Clemens NT, Dolling DS (2009) Active control of supersonic inlet unstart using vortex generator jets. In: 39th fluid dynamics conference and exhibit, San Antonio, TX, USA

Wagner JL, Yuceil KB, Valdivia A, Clemens NT, Dolling DS (2008) PIV measurements of the unstart process in a supersonic inlet/isolator. In: 38th fluid dynamics conference and exhibit, Seattle, WA, USA

Wagner JL, Yuceil KB, Clemens NT (2009a) PIV Measurements of Unstart of an Inlet-Isolator Model in a Mach 5 Flow. In: 39th fluid dynamics conference and exhibit, San Antonio, TX, USA

Wagner JL, Yuceil KB, Valdivia A, Clemens NT, Dolling DS (2009b) Experimental investigation of unstart in an inlet/isolator model in Mach 5 flow. AIAA J 47:1528–1542

Wang X, Le J (2000) Computations of inlet/isolator for SCRAMjet engine. J Thermal Sci 9:334–338

Wieting AR (1976) Exploratory study of transient unstart phenomena in a three-dimensional fixed-geometry scramjet engine. NASA Technical Note: TN D-8156

Wu P, Lempert WR, Miles RB (2000) Megahertz pulse-burst laser and visualization of shock-wave/boundary-layer interaction. AIAA J 38:672–679